Journal of Catalysis **199,** 92–106 (2001)
doi:10.1006/jcat.2000.3122, available online at http://www.idealibrary.com on IDEAL®

Predictions of Relationships between Catalytic and Solid Phase Properties by Kinetic Models and Their Validation

Dorit Wolf,[1] Martin Heber, Wolfgang Grünert, and Martin Muhler

Lehrstuhl für Technische Chemie, Ruhr-Universität Bochum, D-4780 Bochum, Germany

Received July 31, 2000; revised November 21, 2000; accepted November 23, 2000; published online February 27, 2001

The paper illustrates that realistic predictions about steady-state coverages and stability of surface species can be obtained by kinetic analysis. As an example, oxidative coupling of methane to ethane over CaO/CeO_2 catalysts is considered. For this reaction, it was earlier predicted by a kinetic model that the steady-state surface coverage with OH groups, oxygen, and vacant sites depends on the CaO content of the mixed oxide catalysts. Now, the surface of solid solutions of CaO in CeO_2 (5, 10, and 20 mole % CaO), in which the incorporation of Ca into the CeO_2 host lattice can be demonstrated by pronounced effects on the electrical conductivity, has been characterised by XPS, UPS, ISS, and IR techniques. It was found that bulk and surface properties are interrelated but do not change proportionally. The oxygen anion conductivity increases and a change from *n*- to *p*-type conductivity occurs with increasing CaO-content. The external surface of the mixed oxides is strongly enriched in CaO, which forms $CaCO_3$ under ambient conditions, but the degree of surface enrichment exhibits a marked minimum at 10% CaO. As predicted by former kinetic analysis in the oxidation of methane, this sample is capable of forming surface OH groups of exceptional thermal stability. © 2001 Academic Press

INTRODUCTION

The importance of kinetic analysis as a tool to elucidate catalytic reaction mechanisms and to predict optimal catalyst performance was recently emphasized by Boudart (1). For catalytic processes occurring on metal surfaces, information about electronic and atomic surface processes are available from surface science studies to a large extent (2). However, for polycrystalline catalysts with complex structures (e.g., mixed oxides), the identification of the surface and bulk structures which are relevant for catalysis and the determination of the kinetic parameters on an elementary-step level are still unsolved problems, since contributions of surface and bulk to catalytic reactions cannot easily be separated and their structure can change with increasing degree of conversion as well (3).

The set-up of mechanistically based kinetic models, for which kinetic constants are derived by fitting the model predictions to the experimental results of catalytic studies, is a pragmatic approach to overcoming the present lack of information about elementary steps on complex polycrystalline catalysts. In contrast to conventional kinetic rate equations of Langmuir–Hinshelwood (4), Eley–Rideal (5), or Hougen–Watson type (6), mechanistically based models must not be simplified by assuming rate-determining reaction steps. In this way, crucial reaction steps which affect the overall rate and selectivity can be identified, their rates can be determined, and their changes due to gradual modifications of catalyst properties, such as quantitative ratio of active components and amount of promoters, can be elucidated. Hereby, feedback to catalyst design under conditions close to those of the technical processes will be obtained.

The procedure of kinetic analysis, however, requires a suitable basis of experimental data under steady-state as well as under non-steady-state conditions, leading to significant estimates of rate constants. Moreover, a robust numerical tool for parameter estimation has to be used. To judge whether parameters are significant, sensitivity and correlation analyses have to be performed. This strategy of kinetic data analysis was already applied to the oxidative coupling of methane over CaO/CeO_2 catalysts (7). The numerical tools for parameter estimation and correlation analysis used are described in (8, 9).

In our former study of the CaO/CeO_2 system (7), the kinetics of oxidative methane coupling over catalysts with different Ca content was analysed and information on the relationship between rate constants of surface reaction steps and catalyst composition was derived. This led to predictions of steady-state coverages by surface OH-groups, molecularly adsorbed oxygen species, and lattice oxygen. Surprisingly, the predicted steady-state coverages did not correlate with the bulk composition of the catalyst for each type of surface species (i.e., for OH groups). Moreover, the discontinuities in the kinetic constants were not found in the integral values of ethane selectivity and CH_4 conversion observed in our catalytic experiments. Thus, the question of

[1] To whom correspondence should be addressed. Current address: Institut für Angewandte Chemie Berlin-Adlershof e. V., Richard-Willstätter-Str. 12, D-12489 Berlin, Germany.

0021-9517/01 $35.00
Copyright © 2001 by Academic Press
All rights of reproduction in any form reserved.

whether the rate constants reflect the real surface processes arose.

The present paper reports an effort to analyse the surface structure of CaO/CeO_2 mixed oxides, as well as its interplay with bulk properties, by spectroscopic and diffraction techniques (electron microprobe analysis, XRD, X-ray and ultraviolet photoelectron spectroscopy (XPS, UPS), ion-scattering spectroscopy (ISS), and IR spectroscopy (diffuse reflectance mode, DRIFTS)) in order to validate these unexpected model predictions. Furthermore, bulk defect properties of the mixed oxides were investigated by measuring the electrical conductivity at 1123 K at varying oxygen partial pressure (discrimination between electron and oxygen-anion conductivity).

SUMMARY OF EARLIER KINETIC ANALYSIS AND MODEL PREDICTIONS

First, the results of kinetic analysis are briefly summarised and complemented with information on advances in the modelling procedure meanwhile obtained.

The experimental set-up of the former kinetic study in a tubular flow reactor system operated under steady-state conditions was described in (7). In this study, the evaluation of kinetic constants for crucial reaction steps in the oxidative methane coupling over CaO/CeO_2 catalysts was based on the following reaction scheme (with $[\ ]_{(s)}$ stands for surface anion vacancy):

$$CH_{4(g)} + [O]_{(s)} \underset{1'}{\overset{j_E\ 1}{\rightleftarrows}} CH_{3(g)} + [OH]_{(s)}$$

$$CH_{3(g)} + [O]_{(s)} \xrightarrow{2} CH_3O_{(g)} + [0\ ]_{(s)}$$

$$\xrightarrow{+O_2\,(gas\text{-}phase,\ fast)} \cdots CO_{x(g)} + [\ ]_{(s)}$$

$$2[OH]_{(s)} \xrightarrow{3} H_2O_{(g)} + [O]_{(s)} + [\ ]_{(s)}$$

$$O_{2(g)} + [\ ]_{(s)} \underset{4'}{\overset{4}{\rightleftarrows}} [O_2]_{(s)}$$

$$[O_2]_{(s)} + [\ ]_{(s)} \xrightarrow{5} 2[O]_{(s)}$$

$$2CH_{3(g)} \xrightarrow{6} C_2H_{6(g)}$$

$$C_2H_{6(g)} + [O_2]_{(s)} \xrightarrow{7} 2CH_3O_{(g)} + [\ ]_{(s)}$$

$$\xrightarrow{+O_2\,(gas\text{-}phase,\ fast)} \cdots 2CO_{x(g)} + [\ ]_{(s)}.$$

In order to simulate the molar rates of reactant component change the reactor was described as an isothermally operating tubular plug-flow reactor. Assuming steady-state conditions for the reaction and the validity of the perfect gas law, the material balance for the gas-phase species (CH_4, O_2, C_2H_6, C_2H_4, CO, CO_2, and H_2O) is

$$\frac{d\dot{n}_i}{dm_{cat}} = \sum_j \upsilon_{ij} r_j. \qquad [1]$$

(See Appendix: Nomenclature for meaning of symbols.) This system of differential equations was integrated numerically by a Gear algorithm (10). For the steady state of the reactor, the mass balance of the surface species yields a system of nonlinear equations:

$$\frac{d\theta_i}{d(m_{cat}/\dot{V}^0)} = 0 = \frac{N_A}{Z \cdot A_{BET} \cdot \rho_{cat}} \sum_j \upsilon_{ij} r_j$$

$$= \sum_j \upsilon_{ij} k_j \left(\prod_m \theta_{mj}^{a_{mj}} \prod_n p_{nj}^{b_{nj}} \right). \qquad [2]$$

Accordingly, the steady-state surface coverages θ_i (for $[O_2]$, [O], [OH], [ ]) resulted from the numerical solution of this set of nonlinear equations and the balance of normalised surface coverages θ_i of the oxide surface.

Two points have meanwhile resulted in advances in the kinetic analysis as compared with that it (7):

(A) As before, for the calculation of the methyl radical concentration, Bodenstein's principle of quasi-steady state was applied. However, in a re-evaluation of the data, the formation of a concentration gradient within the boundary layer between catalyst surface and gas phase was also considered:

$$0 = k_6 p_{CH_4} \theta_0 - k_{6'} p_{CH_3} \theta_{OH} - 2k_6 p_{CH_3}^2$$

$$- \frac{D_{CH_3}}{RT \varepsilon_{cat} \rho_{cat}} \frac{\partial^2 p_{CH_3}}{\partial \delta^2}. \qquad [3]$$

The rate constant of methyl radical recombination (k_6) was now taken from (11) and not determined by parameter estimation. Several parameter correlations (see below) were avoided by these changes in the procedure of kinetic parameter estimation, which explains the changes in the absolute values of re-evaluated rate constants compared to those presented in (7). However, the agreement between experimental and calculated data was identical for both models, the relationships between values of rate constants and catalyst composition (CaO content) and especially, the irregularities concerning the formation and removal of surface species were preserved. The re-evaluated data are summarised in Fig. 1.

(B) An uncertainty in the earlier kinetic study resulted from the fact that no correlation analysis of the kinetic parameters was performed. However, any analysis of relationships between kinetic parameters and catalyst properties can be reliable only on the basis of information that contains an assessment of parameter significance and correlation. The results of the analysis performed now are illustrated

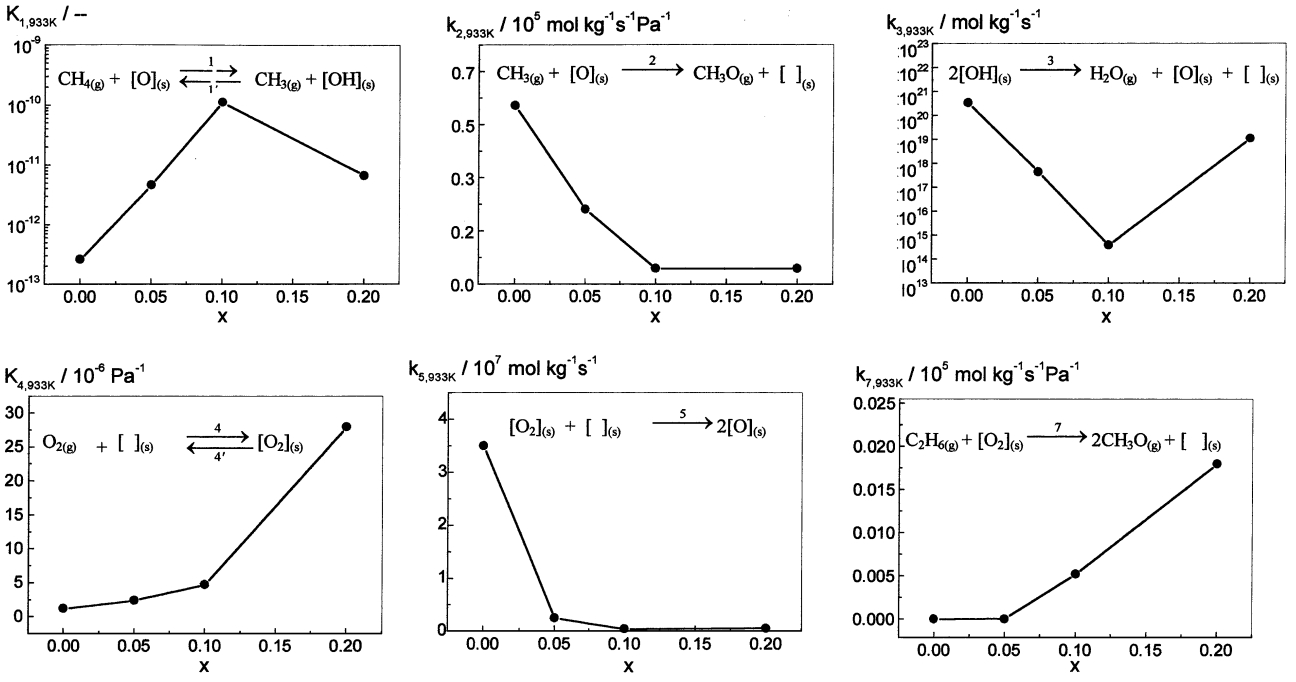

FIG. 1. Kinetic and equilibrium constants for reaction steps $j = 1, \ldots, 7$ depending on the molar ratio $x = n_{Ca}/(n_{Ca} + n_{Ce})$ of the catalysts.

for one catalyst composition (20% CaO/CeO_2) in Fig. 2. The contour lines in Fig. 2 are functions of the particular kinetic constants changed in the pair. The contour lines indicate constant levels of the residual values (sum-of-square values) which corresponds to deviations between experimental kinetic data and those predicted by the kinetic model. If closed minimum regions, i.e., closed contour lines, are obtained the respective rate constants are independent from each other (not correlated). If open valleys are observed the single values of rate constants are not significant and one parameter can be expressed by a functional relationships of the other one. Then, the two kinetic parameters are correlated. In Fig. 2, most of the rate constants show indeed closed minima. However, there are two exceptions: Straight open valleys were found for forward and reversed rate constants k_1 and $k_{1'}$ (methane dissociation) as well as k_4 and $k_{4'}$ (oxygen adsorption). In these cases, only the ratios $k_1/k_{1'}$ and $k_4/k_{4'}$ are significant. In general, such linear correlations indicate fast equilibration of the corresponding reaction steps.

Except for reaction step 6, the model does not include details of the gas-phase reactions of radical intermediates. Therefore, it is only valid in the range of low reaction temperatures (<950 K) where the surface processes dominate the product distribution. Since a consecutive step of oxidative dehydrogenation of ethane to ethylene is not considered in the model it is restricted to the range of low conversion where this step does not occur to a significant extent ($\tau < 0.015\ g\ s^{-1}\ ml^{-1}$, $X(CH_4) < 10\%$, $X(O_2) < 30\%$, $C_2H_4/C_2H_6 < 0.1$). However, these limitations were intended to focus our kinetic study on the primary catalytic reaction steps. In this range of reaction conditions the experimental data were adequately described.

For the present considerations of relationships between catalyst structure and values of rate constants only the significant values of kinetic constants are taken into account. From Fig. 1, it becomes obvious that kinetic rate constants for each reaction step do not change with catalyst composition in an uniform manner. On one hand, there are rate constants the values of which are correlated with the nominal bulk composition (these are oxygen adsorption equilibrium ($j = 4, 4$), oxygen incorporation into the lattice ($j = 5$), and oxidation of methyl radicals ($j = 2$) and ethane ($j = 7$). On the other hand, there are reaction steps which obviously do not parallel the nominal catalyst composition, such as the reversible dissociation of methane ($j = 1, 1$) and the surface dehydroxylation ($j = 3$). The maximum in K_1 and the corresponding minimum in k_3 at a CaO content of 10 mole % would imply that for this particular catalyst composition an exceptional ligh surface coverage and high stability of surface OH-groups have to be expected under steady-state conditions of the reaction.

The present paper intends to explain the structural reasons of the different relationships presented in Fig. 1 by means of analysis of surface and bulk composition.

EXPERIMENTAL

Catalyst preparation. Solutions of CaO in CeO_2 (molar ratio $x = n_{Ca}/(n_{Ca} + n_{Ce}) = 0$–0.20) were prepared by

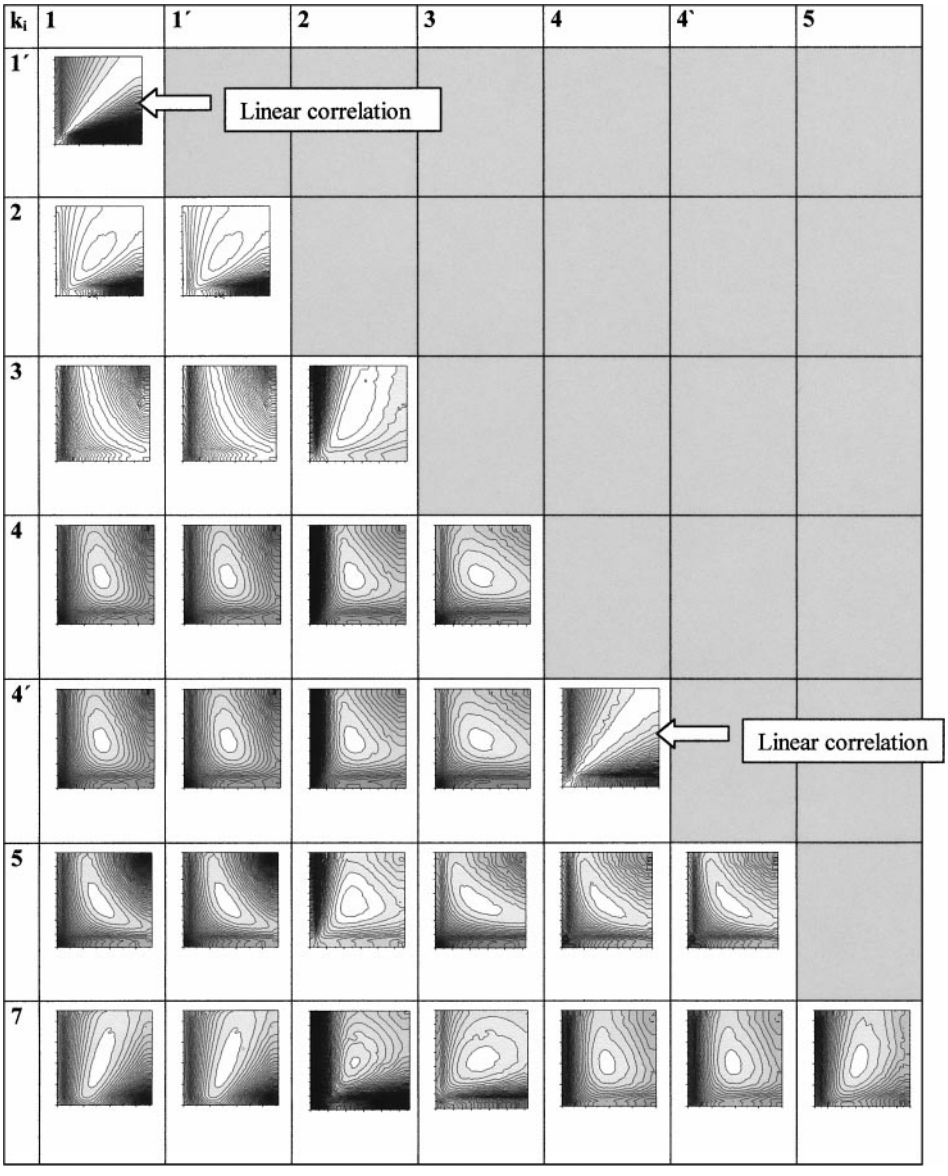

FIG. 2. Pairwise sum-of-square contours of rate constants $j = 1, \ldots, 7$, excluding k_6, which was not adjusted but taken from the literature [11]. Each constant was varied in the range $0.1k_i \leq k_i \leq 2k_i$; the inner contour lines correspond to the minimum region at the confidence level of 90%.

co-precipitating the oxalates from a continuously stirred solution of calcium and cerium nitrates with 1 M oxalic acid at room temperature. The precipitate was stirred for two more hours and was then allowed to settle overnight. Subsequently, it was filtered and washed with oxalic acid. Finally, it was dried at 393 K for 4 h and calcined at 1123 K for 24 h in ambient air. The materials obtained had a BET surface area between 1.9 and 2.3 $m^2\ g^{-1}$ (determined by a one-point BET technique).

Electron microprobe analysis (EPMA). The sample composition (Ca content) was confirmed applying an energy-dispersive X-ray diffractometer (Kevex/Röntec DER 288). The acceleration voltage amounted to 25 kV.

XRD. Crystalline phases were analysed with a Phillips PW 1710 X-ray diffractometer applying CuK_α radiation. The catalysts were investigated without any pretreatment.

Electrical conductivity measurement. The overall conductivity σ (*n*- and *p*-type and oxygen anion conductivity) was determined by measuring the specific resistance of a catalyst disc by the two-electrode AC method (12). For this purpose, AC (1-kHz) measurements were performed with an automatically compensating bridge (Wayne Kerr B905) with two inert platinum electrodes arranged in a quartz cell as described in (13).

The ground powders were pressed into pellets of diameter 7 mm at a pressure of 2.2×10^5 kPa. To minimise

contact resistance the discs were covered with a platinum paste on each side and fired at a temperature of 1023 K for 30 min. AC conductivity measurements were carried out at varying oxygen partial pressures ($p_{O2} = 0.1$–31.6 kPa) at 1123 K. Since solid solutions may exhibit several types of conductivity simultaneously (*n*- and *p*-type and oxygen-anion conductivity) the prevalent conductivity type was derived from the change of the overall conductivity upon variation of the oxygen partial pressure (cf. (13)). *p*-type conductivity can be concluded when the conductivity increases with increasing partial pressure of oxygen ($\delta\sigma/\delta p_{O2} > 0$), while *n*-type conductivity is indicated by a decreasing slope ($\delta\sigma/\delta p_{O2} < 0$). In an intermediate range of oxygen partial pressure, oxygen anions can be the dominant charge carriers, resulting in constant conductivity at varying oxygen partial pressure.

Surface analysis. XPS, UPS, and ISS measurements were performed with Leybold surface analysis systems (most of XPS, ISS: LHS 12 spectrometer[2] equipped with an EA 200 multichannel detector; UPS, confirmative XPS, ISS: LHS 10 spectrometer equipped with an EA 10/100 multichannel detector). The base pressure of the analysis chamber was $<1 \times 10^{-9}$ mbar in both cases. The powdered samples were ground, deposited onto a stainless-steel sample holder from a slurry of *n*-hexane, and mounted on the sample rod. Sample pretreatment could be done either in the fast entry lock or in two adjacent high-vacuum preparation chambers. Transfer to UHV was managed without exposing the samples to the ambient atmosphere.

XP spectra were measured with nonmonochromatised Mg$K\alpha$ radiation and recorded at a constant analyser pass energy of 108 eV. The samples were studied in the as-received state, after being noted to 823 K *in vacuo* and after He-ion scattering. The wide-range spectra showed no impurities except adventitious carbon. The XPS binding-energy (BE) scale was referred to Ce $3d_{5/2}$ ("adiabatic transition") = 882.0 eV. With this calibration, C l*s* was found in the range 284.2–284.8 eV with only some exceptions (cf. Table 2) whereas the binding energy of the lattice-oxygen peak was found in a narrow BE range of 528.8–529.1 eV. Hence, we conclude that the Ce 3*d* secondary binding-energy standard did not obscure any relevant tendency. Prior to further numerical treatment of the spectra, the X-ray satellites were carefully removed and the background was subtracted assuming a Shirley-type background function (14). Atomic ratios were calculated from line intensity ratios using the empirical sensitivity factors by Wagner *et al.* (15).

UP spectra were measured with HeII excitation (40.82 eV). Due to the low kinetic energy of the photoelectrons, surface charging is deleterious for UPS; hence, samples must exhibit sufficient electrical conductivity to provide the sample current from the spectrometer to the sample surface. For the materials under investigation (except for molar ratio $X = n_{Ca}/(n_{Ca} + n_{Ce})) = 0.20$) this was achieved by performing the UPS measurements at elevated temperatures ($T \geq 773$ K).

IS spectra were acquired using He^+-ions of primary energy 1000 eV and measured at a constant analyser pass energy of 192 eV, with a scattering angle of 135°. Typically 20 spectra were recorded for each sample, the first 10 with an ion current of 0.5 μA, the remaining ones with 1.5 μA. Sample charging was compensated for by using a low-energy flood gun. Numerical analysis was performed by integrating the peaks after subtraction of a linear background. The ISS series were performed with samples that had been heated in vacuum at 823 K before.

DRIFTS. For DRIFTS analysis, a Unicam RS FTIR spectrometer equipped with a diffuse reflection cell (Spectra-Tech Mod. 0030-103) and a mercury cadmium telluride detector cooled by liquid nitrogen was applied. The reaction chamber consisted of a ceramic sample holder that was electrically heated and covered by a dome made of stainless steel with ZnSe windows. Temperatures were measured with a thermocouple located in the catalyst bed. During temperature-programmed surface dehydroxylation, 200 scans were recorded per spectrum (4 cm^{-1} resolution, total acquisition time ≈45 sec). For steady-state in-situ spectra (methane oxidation), 400 scans were accumulated at a resolution of 2 cm^{-1}.

RESULTS

Bulk Structure and Defects

The X-ray diffractograms of the mixed-oxide samples exhibited CeO_2 as the only crystalline phase (cf. Table 1). The lattice parameters were unaffected by the presence of various amounts of calcium.

Figure 3 reports the results of the AC conductivity measurements with the CaO/CeO_2 samples in a plot of log σ versus the oxygen pressure of the gas phase. Pure

TABLE 1

Properties of CaO/CeO_2 Model Catalysts

	Nominal molar ratio $x\ (= n_{Ca}/(n_{Ca}+n_{Ce}))$			
	0	0.05	0.10	0.20
Measured x (EPMA)	—	0.052	0.092	0.203
Weight loss, wt.% (873 K, 3×10^{-5} Pa)	0.12	0.87	1.33	3.14
Crystalline phases (XRD)	CeO_2	CeO_2	CeO_2	CeO_2
BET surface area, $m^2\ g^{-1}$	2.0	2.3	1.9	2.0
Type of electrical conductivity	*n*	*n* (weak)	O^{2-}-ion	O^{2-}-ion and *p* (weak)

[2] Spectrometer located at the Fritz-Haber Institut of the Max Planck Gesellschaft in Berlin.

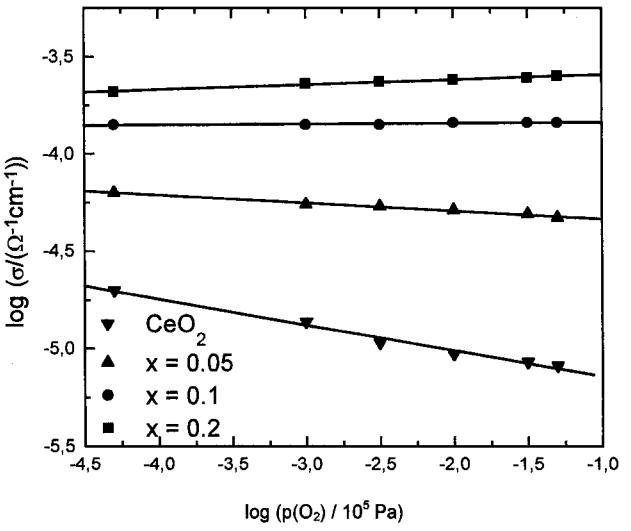

FIG. 3. Overall electrical conductivity at varying oxygen partial pressure at 1123 K.

CeO_2 shows only *n*-type conductivity ($\delta\sigma/\delta p_{O2} < 0$). Upon addition of small amounts of Ca ($x = n_{Ca}/(n_{Ca} + n_{Ce}) = 0.05$), the overall conductivity increases markedly while its decay with growing oxygen partial pressure decreases. This indicates that a diminished *n*-type contribution is now superimposed by oxygen-anion conductivity. With increasing Ca content, the overall conductivity keeps on growing. However, the slope decay with growing oxygen partial pressure changes its sign, with a zero-slope dependence around $x = 0.10$. Obviously, the type of conductivity superimposed on the increasing oxygen-anion conductivity changes with increasing Ca content from *n*- to *p*-type. At $x = 0.10$, the electron conductivity is negligible, rendering the sample a practically pure oxygen-anion conductor (cf. Table 1).

Surface Properties

XPS. Figure 4 shows typical XPS signals shapes of the Ce 3*d*, O 1*s*, and C 1*s* lines as observed in the present study. The spectral parameters are summarised in Table 2.

In the initial state and after heating, the Ce 3*d* line always exhibited a shape close to that known for CeO_2 [16]. No significant influence of Ca admixture on the Ce 3*d* signal shape was noted, but such influence would have been difficult to detect since the general line width varied significantly with the amount of surface charging as revealed by the width of the u''' satellite feature. For this reason, our discussion of Ce^{4+} reduction will be based on the contribution of this feature to the total Ce 3*d* intensity (16, 17). Since Ce^{3+} compounds do not exhibit the u''' satellite, its contribution to the total signal area decreases with increasing reduction degree of ceria. As expected, it decays slightly upon evacuation at 823 K, and further during ISS (Table 2). After ISS, the line shapes were in general broader and tended to be distorted. Hence, for the surface state after ISS, only intensity data will be discussed in this paper.

The Ca 2p binding energy was found in the range typical of CaO and $CaCO_3$ (347.3, 347.0 eV (17)), the latter also confirmed by an own reference measurement) or slightly below it. The O 1*s* lines were asymmetric and could be fitted by two components. The major component, denoted as O_L, had a binding energy of 529.0 ± 0.1 eV, while the minor component was found at a BE of 531.9 ± 0.2 eV, with the sole exception of CeO_2 after thermoevacuation. Analogously, two C 1*s* signals could be discerned in all spectra.

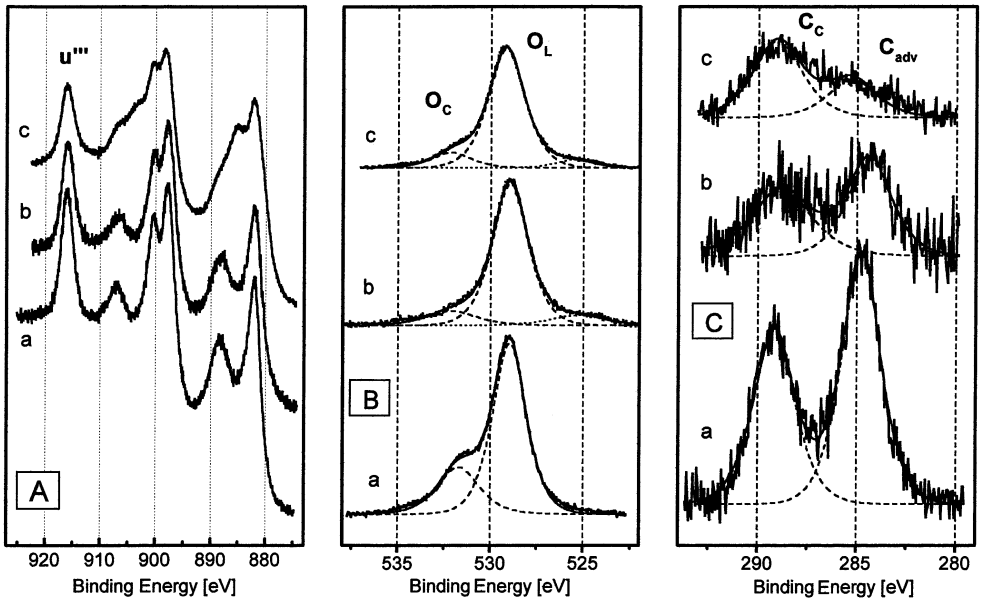

FIG. 4. Typical XPS signal shapes measured with CeO_2 and CaO/CeO_2 mixed oxides (example; CaO/CeO_2, $x = 0.10$). (A) Ce 3*d*, (B) O 1*s*, (C) C 1*s*; (a) as-received, (b) after evacuation at 823 K, 1 h, (c) after ISS.

TABLE 2

XPS of CeO_2 and CaO/CeO_2 Mixed Oxides: Binding Energies (eV) and Surface Atomic Ratios

Sample	Line	Code	As rec.	Vac, 823 K	After ISS
CeO_2	Ce 3*d*: *u‴*/total area[a]		0.121	0.117_5	0.088
	O 1*s*: BE, [*n*(O)/*n*(Ce)]	O_L	529.0 [1.7]	529.0 [1.5]	529.0 [1.5]
		O_C	531.8 [0.2]	530.6 [0.15]	(531.3 [0.25])
	C 1*s*: BE, [*n*(C)/*n*(Ce)]	C_{adv}	284.2	284.2	284.7_5
		C_C	288.6 [0.15]	288.8 [0.1]	289.2 [0.2]
$x = 0.05$[b]	Ce 3*d*: *u‴*/total area[a]		0.120	0.116	0.097
	Ca $2p_{3/2}$: BE, [*n*(Ca)/*n*(Ce)]		347.2 [0.45]	347.2 [0.40]	346.9 [0.25]
	O 1*s*: BE, [*n*(O)/*n*(Ce)]	O_L	528.8 [2.3]	529.1 [2.3]	529.1 [1.8]
		O_C	531.7 [1.4]	532.0 [0.9]	531.9 [0.6]
	C 1*s*: BE, [*n*(C)/*n*(Ce)]	C_{adv}	284.9	285.2	285.6
		C_C	289.3 [0.6]	289.5 [0.5]	289.4 [0.25]
x = 0.05[c,d]				(vac 923 K)	({vac 923 K}[e])
	Ce 3*d*: *u‴*/total area[a]				
	Ca $2p_{3/2}$: BE, [*n*(Ca)/*n*(Ce)]		347.0 [0.35]	346.4 [0.35]	346.0 [0.33]
	O 1*s*: BE, [*n*(O)/*n*(Ce)]	O_L	528.8 [3.0]	529.0 [2.3]	528.8 [3.0]
		O_C	531.5 [1.1_5]	531.3 [0.8]	531.7 [0.2]
	C 1s: BE, [*n*(C)/*n*(Ce)]	C_{adv}	284.6	284.4	284.2
		C_C	289.1 [0.65]	289.0 [0.3]	288.5 [0.35]
$x = 0.10$	Ce 3*d*: *u‴*/total area[a]		0.118	0.113_5	0.093
	Ca $2p_{3/2}$: BE, [*n*(Ca)/*n*(Ce)]		346.9 [0.18]	346.7 [0.16]	346.4 [0.10]
	O 1*s*: BE, [*n*(O)/ *n*(Ce)]	O_L	528.9 [2.2]	528.9_5 [1.9]	529.0 [1.6]
		O_C	531.7 [0.6]	532.3 [0.2]	532.0 [0.2]
	C 1*s*: BE, [*n*(C) /*n*(Ce)]	C_{adv}	284.7	284.5	285.1
		C_C	289.1 [0.3]	289.0 [0.15]	288.9 [0.15]
$x = 0.20$	Ce 3*d*: *u‴*/total area[a]		0.126	0.119	0.101
	Ca $2p_{3/2}$: BE, [*n*(Ca)/*n*(Ce)]		347.3 [1.50]	346.6 [1.40]	346.8 [0.80]
	O 1*s*: BE, [*n*(O)/ *n*(Ce)]	O_L	528.8_5 [3.4]	529.0 [3.5]	529.1 [2.4]
		O_C	531.7 [4.55]	532.0 [1.0]	531.9_5 [0.7]
	C 1*s*: BE, [*n*(C)/ *n*(Ce)]	C_{adv}	284.8	284.7	285.4
		C_C	289.5 [1.4]	289.6 [0.3]	289.4 [0.3]

[a] See Fig. 5.
[b] Batch I.
[c] Batch II.
[d] Ca/Ce ratio after vac, 1123 K: 0.45.
[e] Vac 923 K, 2 h + H_2, room temperature, 30 min + vac 923 K, 2 h.

The composition of the XPS sampling region exhibits some pronounced tendencies, which can be derived from Table 2. The Ca/Ce atomic ratios near the external surface were always larger than in the bulk (cf. Table 1). Notably, the extent of surface enrichment was lowest at $x = 0.10$ (10% CaO/CeO_2). After sputtering, the Ca/Ce ratio decreased significantly. It came close to the bulk value for $x = 0.10$, but still indicated significant Ca enrichment with the remaining mixed oxides ($x = 0.05$; 0.20). As there seems to be a small, hardly significant tendency of the Ca/Ce ratio to decrease upon thermoevacuation at 823 K, a sample with $x = 0.05$ was thermoevacuated at higher temperatures (923 K; 1123 K). The results reported in Table 2 clearly exclude the Ca enrichment of the sampling region decreasing upon calcination.

For all calcium-containing samples, the atomic ratio between O_C and Ca was close to 3 in the initial state, but decreased upon heating and/or sputtering. Since both O_C and C_C arise from carbonate (see below), a Ca/C_C stoichiometry of 1 would be expected, but the experimental data showed considerable deviations from this value.

ISS. Figure 5 shows IS spectra as typically measured with the CaO/CeO_2 samples (example: $x = 0.10$). Scans taken after different measurement times (i.e., different ion doses applied to the sample) are compared. As ISS is a sputtering technique, these spectra compare compositions at different distances from the external surface. It can be seen that Ca is highly enriched at the external surface. Upon sputtering, the Ca peak decreases strongly, and the Ce peak grows. The oxygen peak is not well-shaped in all the samples investigated, as has often been observed in oxides of heavy elements (M. Heber, S. Sprenger, W. Grünert, and M. Muhler, unpublished results).

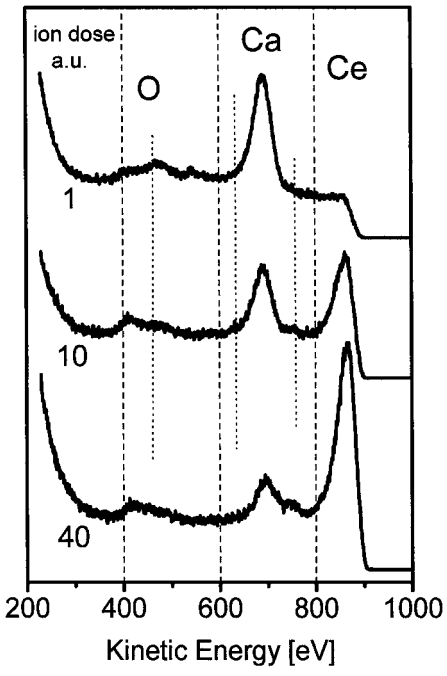

FIG. 5. ISS sputter series with a CaO/CeO_2 sample ($x = 0.10$, after previous evacuation at 823 K): development of spectrum with increasing ion dose.

Figure 6 summarises the ISS sputter series measured with the Ca–Ce mixed oxides. Ca and Ce peak areas from runs, in which the sample area and analysis conditions were unchanged, are plotted in the figure.

The step in each curve, which is marked by a dotted vertical line, is due to a change in the primary ion current as described under Experimental. The curves can be taken as (qualitative) concentration profiles from the external surface towards the bulk, where the final sputtering depth was estimated to be 4–5 monolayers from the ion doses applied and sputter yields tabulated in (18). A decay of the Ca signal corresponding to an increase of the Ce signal, was found for all samples. At $x = 0.20$, the Ce signal was hardly detectable in the first ISS scan. At $x = 0.10$, the majority component Ce increased most steeply and became constant (within experimental error) after half of the total ion dose applied, while at $x = 0.20$ and 0.05, the Ce signal went on growing all the time. As Ce constitutes 80–95% of the bulk cations, such increasing tendency can be measured only if the composition of the probed surface is still far from the bulk composition. For the same reason, the surface composition of the third sample ($x = 0.10$) should have come close to the bulk composition after sputtering since any change still occurring is detectable only for the minority Ca component but is below the detection limit for Ce.

UPS. UP spectra measured with CeO_2 and CaO/CeO_2 mixed oxides are displayed in Fig. 7. In all cases, the spectra denoted by a are the as-received state, which has, however, been subjected to ultrahigh vacuum at 773 K to allow the acquisition of the UP spectrum.

It can be seen that the replacement of only 5% of the Ce ions by Ca perturbs the UP spectrum greatly. The spectrum of CeO_2 consists of a strong signal at 4–4.5 eV, with a pronounced shoulder at higher BE, and a small signal at $\approx$2 eV, which is due to valence *f*-electrons on Ce^{3+} ions. At $x = 0.05$, the main peak appears at 6.5 eV while the shoulder is at the lower binding-energy side. In addition, there

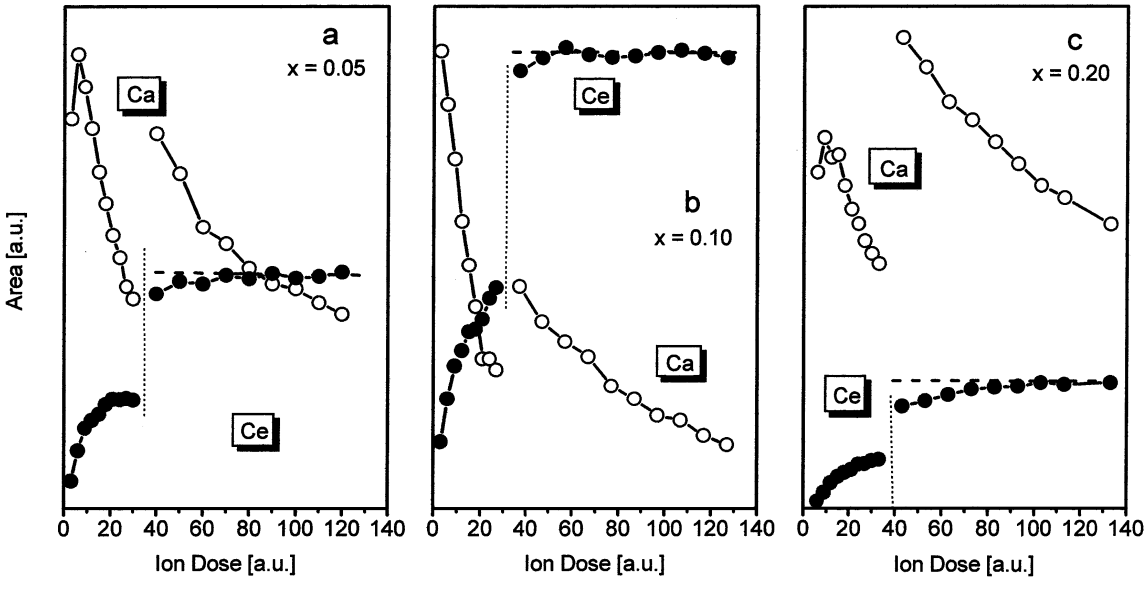

FIG. 6. Development of ISS signal intensities with increasing ion dose for CaO/CeO_2 mixed oxides of different composition (a) $x = 0.05$, (b) $x = 0.10$, (c) $x = 0.20$.

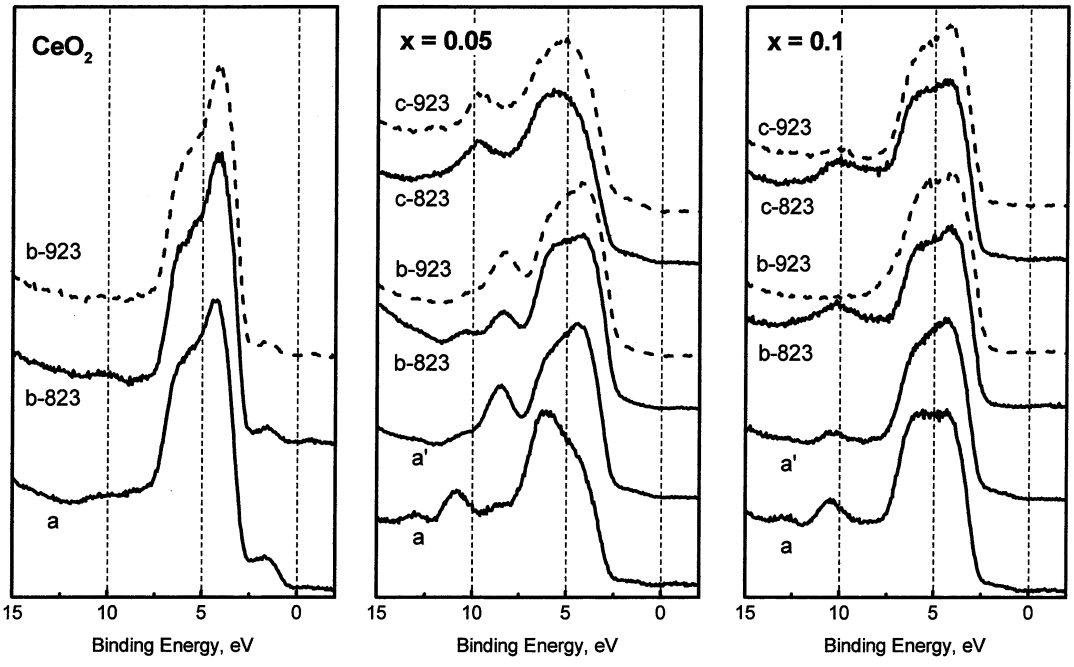

FIG. 7. UP spectra of CeO_2 and CaO/CeO_2 mixed oxides after different treatments: (a) as-received state; (a′) after evacuation at 923 K until no further changes were detectable; (b-823) state a′ (oxidised CeO_2), treated in H_2 at room temperature, measured at 823 K; (b-923) as b-823 K, measured at 923 K; (c-823) state a′, treated in moist air (saturated under ambient conditions) at 573 K, measured at 823 K; (c-923) as c-823 K, measured at 923 K.

are signals at 8.6, 10.9, and 13.1 eV. The latter two signals are also present at $x = 0.10$, while the two states at high BE appear with comparable intensity. Signals at a binding energy of ≈10 eV may arise both from carbonate and OH groups (19; see below).

The application of UPS aimed also to study the state and stability of surface OH-groups. To synthesise OH groups deliberately on the surface the samples were outgassed at 923 K until no change in the UPS could be noted (Fig. 7: spectra a′ for $x = 0.05$ and $x = 0.1$). This leads generally to an increase of the signal at ≈4 eV at the expense of the 6.5-eV signal, and in the mixed oxides to a decay of the states between 10 and 13 eV. At $x = 0.05$, the 8.6-eV signal is strongly enhanced by the outgassing procedure while at $x = 0.10$, there is no comparable trend, and the region around 8.5 eV remains flat.

OH groups were synthesised by two different modes of treatment:

(a) treatment of the outgassed samples with hydrogen at room temperature (with CeO_2, the hydrogen treatment was performed after a reoxidation with O_2 at 573 K).

(b) treatment of outgassed mixed-oxide surfaces with moist air (saturated at room temperature) at 573 K.

In Fig. 7, the spectra recorded after these treatments are denoted by (b) and (c), respectively, specified by the temperature during data acquisition (in K, i.e., b-823, b-923). The changes in the spectra are very characteristic in particular with the mixed oxides. At $x = 0.10$, both hydrogen treatment and hydration by water give rise to a strong signal centred at ≈10 eV and an increase in the 6-eV region. At 923 K, these changes are largely reversed, although closer scrutiny reveals some residual intensity at 10 eV (c-923) and a broadening of the main signal by a shift of intensity into the 7- to 8-eV region (b-923). At $x = 0.05$, hydrogen treatment leads only to a slight enhancement at 10 eV while the 8.5-eV signal is attenuated. These changes are also reversed at 923 K. Treatment with water, however, perturbs the spectrum strongly. There is now a strong signal at 10 eV, and the 8.5-eV signal has completely disappeared. Evacuation of the sample at 923 K does not change this situation significantly. With CeO_2, there is a very small signal at 10 eV after hydrogen treatment, which is completely removed at 923 K (Fig. 7: CeO_2, b-923 K).

DRIFTS. To verify the results of the UPS analysis on state and stability of surface OH-groups, FTIR spectra were measured during the temperature-programmed dehydroxylation of CeO_2 and Ca/Ce mixed oxides. The samples were employed after thermal treatment in N_2 at 873 K to remove carbonate and OH groups, which was extended until no further changes in the spectrum could be noted. During cooling, reference spectra were measured at selected temperatures. The OH groups were generated by contacting the cleaned surfaces with H_2 (20 ml/min) at room temperature.

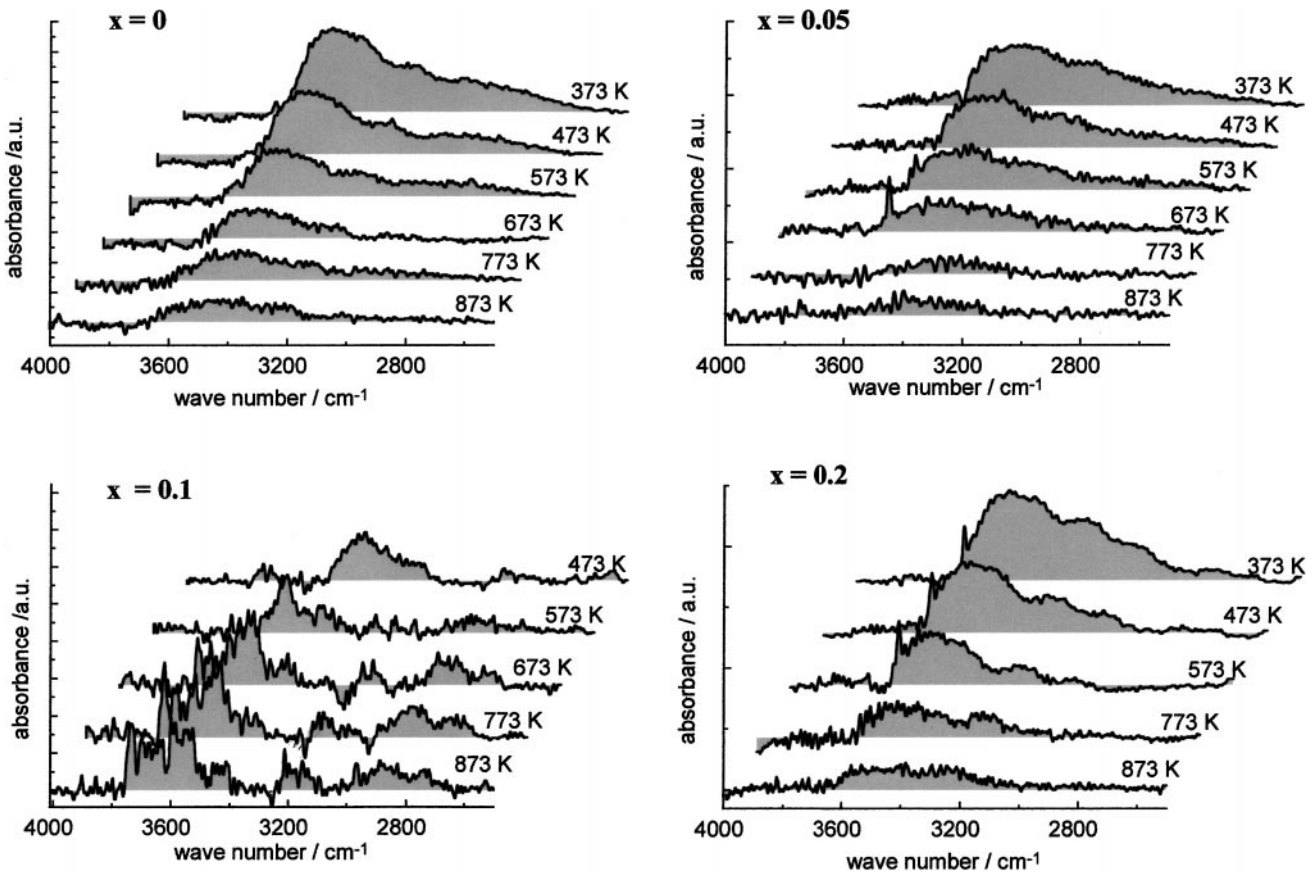

FIG. 8. DRIFT-spectra of surface OH-groups during temperature-programmed dehydroxylation for CeO_2 ($x = 0$) and CaO/CeO_2 mixed oxides ($x = 0.05$, 0.1, and 0.2).

After purging the samples (20 ml/min N_2, until no changes could be detected in the spectra), the temperature-programmed dehydroxylation was performed by increasing the temperatures in 100 K steps to 873 K (Fig. 8).

Due to the high heating rate which was necessary to record the dehydroxylation process for the particular samples in the proper time scale the signal-to-noise ratios are low. Moreover, for $x = 0.1$, a significant change of the baseline during the temperature increase occurred, probably due to formation of F-centres. Therefore, interpretation of the spectra is difficult but should be justified if considered in the context of the UPS data as discussed below.

The broad signal between 2800 and 3700 cm^{-1} in the spectra recorded at 373 K shows that indeed water molecules and OH groups have been formed by the interaction of hydrogen with the surface of the Ce-containing mixtures at room temperature. In calcium-containing materials, bands at higher wave numbers (3400–3700 cm^{-1}) show a high thermal stability. These bands are assigned to isolated OH groups. Contrarily, the associated OH-groups (below 3200 cm^{-1}) are more rapidly removed. While for $x = 0.05$ and 0.20 the broad signal in the 3400- to 3700-cm^{-1} region decays and all sharp OH bands on this background disappear between 573 and 773 K, the intensity in this range seems to increase slightly at $x = 0.10$, and well-resolved OH bands remain in the spectrum even at 873 K (short-time exposure).

DISCUSSION

The experimental results shall be discussed in the context of the prediction of the kinetic model concerning the different dependencies of rate constants of the oxidative conversion of methane on the composition of the CaO/CeO_2 catalyst (see Fig. 1). Especially, the following question have to be answered:

1. Is the Ca indeed incorporated into the CeO_2 lattice?
2. Are there changes of either bulk or surface composition which might explain the maximum for K_1 and the minimum of k_3 (Fig. 1)?
3. Are there indications for an exceptional high stability of surface OH-groups at $x = 0.1$ predicted by the kinetic model?

The answer of the first question was obtained by the combination of XRD and conductivity measurements.

Discrepancies between surface and bulk composition were found by relating the results of bulk analysis to those of surface studies by XPS, ISS, and UPS as discussed further below. Finally, information on the stability of surface OH-groups were derived by UPS and DRIFTS experiments.

Bulk Composition and Defects

X-ray diffractograms were recorded to examine if the incorporation of Ca into the CeO_2 lattice could be proven by lattice parameter changes. While CeO_2 was the only observable crystalline phase in our systems (Table 1), the lattice parameters of the CeO_2 remained unaffected by the admixture of increasing amounts of Ca.

On the other hand, the changes of the electrical conductivity observed upon introduction of CaO (Fig. 3) can be best explained by assuming that Ca has indeed been incorporated into the CeO_2 lattice. While pure CeO_2 shows only *n*-type conductivity, the introduction of Ca into the oxide decreases the (negative) slope in the relation between the conductivity (1g σ) and the oxygen partial pressure. At the same time, the incorporation of Ca creates oxygen vacancies, and the (decreased) *n*-type conductivity is superimposed by a larger contribution of oxygen-anion conductivity, which results in an increased overall conductivity at $x = 0.05$. At $x = 0.10$, the *n*-type conductivity has vanished, and the sample is a nearly pure oxygen-anion conductor. Above $x = 0.10$, the conductivity increases with the oxygen partial pressure, which indicates a superposition of *p*-type conductivity on further increasing oxygen-anion conductivity. The increasing extent of oxygen anion conductivity agrees with results reported earlier by other authors (20, 21). This trend proves the incorporation of an increasing amount of Ca into the CeO_2 host lattice. As mentioned above, the limit of CaO solubility in CeO_2 is at $x \approx 0.20$. Above this value, CaO is formed as a separate phase, which has a low *p*-type conductivity.

Storage of the samples under ambient conditions leads obviously to the formation of $CaCO_3$ in the sample as evidenced by the IR spectra (not shown). Even after calcination of the samples at 923 K in nitrogen some calcium carbonate remained on the surface.

Surface Properties

The XPS binding energies measured with the Ca/Ce mixed oxides (Table 2) agree well with literature data. With Ce 3*d* = 882.0 eV as a BE reference, the main O 1*s* peak, attributed to lattice oxygen, appeared at 529.0 ± 0.1 eV (22: 529.3 eV). The second oxygen signal (O_C) and the high-BE C 1*s* signal (C_C) may be assigned to carbonate and confirm that we have calcium carbonate in the near-surface region.

In the discussion of elemental ratios in the surface layer, it should be noted that with Ce-containing samples, the analysis of the C 1*s* region is complicated by the superposition by a broad Ce line (Ce 4*s*). This tends to render intensity determinations inaccurate, in particular if C 1*s* signals are weak and broad and Ce signals are strong. Cerium amounts have to be evaluated from a line that extends over 40 eV (Ce 3*d*), and it is doubtful if the Shirley approximation used for background subtraction represents the course of the background correctly over this wide range. Nevertheless, some tendencies can be clearly stated, in particular a strong surface enrichment of all mixed oxides in Ca (Table 2, cf. with bulk Ca/Ce ratios in Table 1). Its extent exhibits a remarkable minimum at $x = 0.10$, where it is twofold, while it is ninefold at $x = 0.05$, and 7.5-fold at $x = 0.20$. In this trend, the most unexpected feature is the high surface enrichment at the lowest Ca content. This was, however, confirmed by the control experiment with repeated preparation, as reported in Table 2.

It may be argued that this Ca enrichment is a preparation artefact, occurring during the cooling stage after calcination, where the contact with CO_2 might extract Ca ions from the bulk of the solid solution to allow calcium carbonate formation. If such ion mobility were available at the relatively low temperatures where the carbonate is formed, it should be no problem to reverse the enrichment by destroying the carbonate at high temperatures. Our results show, however, that no decrease of the surface Ca/Ce ratio occurs upon thermoevacuation even at 1123 K. Hence, the Ca enrichment is an intrinsic property of the samples. Upon sputtering with He ions in the ISS experiment, the Ca/Ce ratio decreases according to expectation. The surface exposed by the sputter process (an estimated five monolayers deep in the original sample) has nearly the bulk composition at $x = 0.10$, but is still highly enriched in Ca at $x = 0.05$ and $x = 0.20$.

The ratio between lattice oxygen and Ce (O_L/Ce) in the initial CeO_2 (Table 2) was somewhat below expectation indicating some reduction of the surface. We believe that this deviation is beyond the limits of experimental error, as the ratio of the u''' component in Ce 3*d* to the total signal area, which is indicative of the Ce(III)/Ce(IV) ratio in CeO_2, is below the value of 0.134 given in (16). In the mixed oxides, the O_L/Ce ratio is, however, clearly above the value for pure CeO_2. This is, most likely, due to the fact that the system is not homogeneous as assumed in the calculation of the atomic ratios, but a layered structure, with $CaCO_3$ covering the CaO/CeO_2 solid. In this case, electrons originating from the Ce 3*d* level are more strongly attenuated by the carbonate layer than those from O 1*s* due to their lower kinetic energy. The effect is most pronounced at $x = 0.20$, but least at $x = 0.1$. Upon thermoevacuation and sputtering, the Ce ions become (more) reduced as evidenced by the decreasing tendency of both the u'''/(total area) ratio in Ce 3*d* and the O_L/Ce atomic ratio.

The IS spectra confirm the conclusions from XPS concerning the surface enrichment of Ca. This enrichment is least at $x = 0.10$, and at the end of the sputter series, the surface composition is on the order of the bulk composition because within the limits of experimental accuracy, no more changes can be detected in the majority component Ce. With this state, an estimate of the sensitivity factors in the present ISS experiments may be derived by assuming that the bulk composition has been attained and using the known Ca/Ce ratio of 1/9 to calibrate the Ca/Ce ISS intensity ratio. As the actual Ca/Ce ratio will be somewhat larger than 1/9, such estimate, which is in addition subject to all uncertainties inherent in the quantification of ISS (24) will provide a lower limit of the Ca concentration. On the basis of these assumptions the Ca fraction $x_S(=[n_{Ca}/n_{Ca}+n_{Ce})]_{ISS})$ in the outmost surface layer was estimated to be ≥ 0.85 at $x = 0.10$ after vac, 823 K. For the remaining samples, x_S should be even larger on the basis of both XPS and ISS intensity trends. We refrain, however, from proposing numerical values since our UPS data infer the presence of segregated CaO on these surfaces after carbonate decomposition (19, see below), which should invoke significant shadowing effects in ISS. It is, however, obvious that ISS indicates a more dramatic surface enrichment than XPS since the latter averages over a sampling region in which the extent of enrichment decreases more or less gradually.

The assignment of UPS signals measured with CaO/CeO_2 samples has been discussed in detail in (19) and will be only briefly summarized here. The main UPS signals (cf. Fig. 7) arise from non-bonding oxygen states on lattice oxygen ($\approx$4.5 eV) and Ce–O bonding states ($\approx$6.5 eV). The latter signal obviously contains also contributions from non-bonding O states in OH groups and carbonate, which are shifted to higher BE from the lattice oxygen, as known from the corresponding O 1*s* core level. The peak at 8.6 eV is indicative of CaO. Signals at 11 and 13 eV have been ascribed to carbonate ions, while the peak at 10 eV arises from the 3σ level in the OH group. On this basis we find that the initial surfaces (excluding CeO_2) exhibit indeed carbonate species under UHV at 773 K; i.e., the conditions of data acquisition (Fig. 7: $x = 0.05$, $x = 0.1$, spectra a). As outlined in (19), the behaviour of the 8.5 eV signal reveals a characteristic difference between the samples with $x = 0.05$ and $x = 0.10$. The fact that it is present only in the former, where it increases upon outgassing at 923 K (Fig. 7: $x = 0.05$ a), implies that in this sample, segregated CaO crystallites are supported on the mixed-oxide surface after outgassing, while at $x = 0.10$, such segregation is absent and the crystals are terminated merely by the Ca-enriched solid solution.

The reason for the unexpected relation between bulk and surface composition may be sought in kinetic phenomena during the preparation steps. The co-precipitation may have produced primary cerium oxalate particles coated with calcium oxalate. Although these particles aggregate during the calcination step that reduces the BET surface down to some m^2/g, the external surface made up of formerly primary surfaces may still be enriched in Ca due to a low diffusion rate of the external Ca ions into the mixed-oxide crystal. This assumption explains well the Ca enrichment near the Ca solubility limit ($x = 0.20$); it fails, however, at low Ca content ($x = 0.05$), where the Ca enrichment is almost as strong as at $x = 0.20$.

A tentative explanation for the enrichment at low Ca content and its decrease with increasing Ca concentration in the range $0.5 \leq x \leq 0.10$ refers to studies of the CeO_2 crystal morphology (24, 25). From these investigations, it is known that in CeO_2 prepared from nitrate solution via oxalate precipitation the polar (100)-surface occurs with a remarkably high abundance, exceeded only by the non-polar (111) plane. An explanation for the stabilisation of the polar surface was given by Conesa using theoretical molecular mechanics methods (26). The calculations indicated that the intrinsic instability of the polar anionterminated (100) surface disappears once its surface-oxygen content is properly adjusted. It should be noted that the equilibrium defect structure of CeO_2 contains electron donor sites (Ce^{3+}), allowing the decrease of the surface oxygen content suggested by Conesa. As found in our study of the electrical conductivity, incorporation of Ca creates oxygen vacancies and reduces the density of electron donor sites (Ce^{3+}), which is indicated by the change from *n* to *p*-type conductivity.

Thus, two counteracting effects might be considered in interpreting the calcium enrichment, depending on Ca content in the range $0 \leq x \leq 0.1$:

1. The reduction of electron donor sites decreases the opportunity to stabilise the surface; i.e., calcium incorporation disturbs surface stabilisation. The surface of the mixed oxide phase tends to be depleted in Ca; hence, part of the Ca will be segregated from the surface as binary oxide.
2. Above a certain threshold of calcium concentration, the concentration of oxygen defects becomes high enough to contribute significantly to the surface stabilisation by direct anionic charge reduction. Thus, the incorporation of Ca in the surface region might be thermodynamically favoured.

Concerning our experimental findings, the threshold concentration of calcium related to the change between the two different mechanism of surface stabilisation should appear between $x = 0.05$ (surface stabilisation by electron donor sites) and $x = 0.1$ (surface stabilisation by creation of oxygen defects).

OH Group Stability

Returning to the kinetic study and its predictions concerning the stability of surface OH groups on the particular

samples (see Fig. 1), a hypothesis will be set up which relates the exceptional stability of OH-groups for the sample $x = 0.1$ to the favoured incorporation of Ca in the near-surface region.

The experimental proof for the predicted OH-group stability is based on the interpretation of the UP spectra and on the DRIFTS analysis of temperature programmed surface dehydroxylation.

From the OH-group signals observed in the UP spectra (Fig. 7) it is obvious that Ce^{4+} is reduced during hydrogen treatment at room temperature (spectra b). This should produce mainly OH groups associated with Ce ions, while the water treatment (spectra c) hydrates the whole surface. Indeed, after hydrogen treatment we see a particular strong OH group signal on the mixed-oxide surface with $x = 0.10$ (spectrum b-823). Under the same conditions (UHV, 823 K), the OH group signal is much smaller at $x = 0.05$ or 0 (spectrum b-823).

In the sample $x = 0.1$, hydration by water produced nearly the same effect as interaction with hydrogen (cf. spectra b-823, c-823) while at $x = 0.05$, the water treatment causes the 8.5-eV peak indicative of segregation of CaO crystallites to disappear. In the former case, it makes no difference how the OH groups that cover part of the mixed-oxide surface are produced. In the latter sample, treatment with hydrogen produces OH groups only in those surface regions exposing Ce (in solid solution) while hydration affects the whole surface including the segregated CaO micro-crystals apparently covering part of the original mixed-oxide surface. This effect cannot be observed for $x = 0.1$ since CaO is not segregated on this surface to any significant extent.

The findings from the UPS studies are supported by the results of the DRIFTS study of temperature programmed surface dehydroxylation, which show that the surface of CaO/CeO_2 mixed oxides stabilises OH groups at very high temperatures at intermediate Ca content ($x = 0.10$). The IR bands observed in the hydroxyl region during the temperature-programmed dehydroxylation experiments can be assigned in more detail by reference to earlier IR work dealing with the temperature-programmed reduction of CeO_2 (27, 28). Referring to the abundance of oxygen defects created by thermal treatment in hydrogen under different conditions, Perrichon and co-workers (27) related the wave number of OH signals to differences in the Ce coordination of the OH oscillator. A band at 3710 cm^{-1}, which was observed only below 473 K in flowing oxygen, arises from monodentate OH groups (type I groups); bands at 3650 and 3634 cm^{-1} found at up to 473 K in hydrogen atmosphere (100 Torr) were attributed to bidentate coordination (type II), while OH groups with tridentate coordination (type III) appeared above 573 K at wave numbers around 3500 cm^{-1}. In the mixed $CaO–CeO_2$ oxides bands can arise also from coordination of OH groups to Ca, or mixed coordination to Ca and Ce^{n+}, which results in a multitude of bands which were obviously not well resolved in our spectra.

For $x = 0$, 0.05, and 0.20, only bands with wave numbers below 3600 cm^{-1} were found during temperature-programmed dehydroxylation (Fig. 8); they may be assigned to bi- or tridentate coordination (or mixed coordinations). For $x = 0.10$, high intensities appear even at wave numbers up to 3750 cm^{-1}. Surprisingly, the intensity of these bands grows with increasing temperature up to 873 K. Such behaviour may be explained by a change of the Ce ion coordination on the surface, which should be related to a decrease of the oxygen defect concentration on the surface with increasing temperature. The appearance of bands in this region as a result of a frequency shift is, therefore, an indication of a high oxygen anion mobility. Indeed, the sample $x = 0.1$ shows high contribution of oxygen anion conductivity to the overall electrical conductivity. The effect cannot be observed with CeO_2 and at $x = 0.05$, where the oxygen anion mobility is much lower. At $x = 0.20$, a similar effect would be expected since the oxygen anion conductivity is similar to that at $x = 0.1$. However, it may have been obscured by the almost dense CaO ($CaCO_3$) layer covering the external surface as indicated by XP and IS spectra. On this basis, we conclude that the exceptional behaviour of the 10% CaO/CeO_2 sample concerning the stability of OH groups as well as the degree of Ca enrichment at the external surface found by XPS and ISS studies is governed by the interplay between bulk and surface properties.

CONCLUSIONS

In the present paper, the potential of steady-state kinetic analysis in predicting rates of surface reactions and steady-state surface coverages depending on solid phase properties was analysed for the oxidative conversion of methane over CaO/CeO_2 mixed oxides. For this example, the predicted steady-state coverages cannot be correlated with the nominal bulk composition of the catalyst for each type of surface species (i.e., for OH groups). To elucidate whether these predictions reflect the reality the surface of the CaO/CeO_2 catalysts has been characterised by XPS, UPS, ISS, and IR. The incorporation of Ca into the CeO_2 host lattice has been demonstrated by pronounced effects on the electrical conductivity. It was found that changes in bulk and surface properties are interrelated but not parallel. The external surface of the mixed oxides is strongly enriched in Ca, which forms $CaCO_3$ under ambient conditions, but the degree of surface enrichment exhibits a marked minimum at 10% CaO. Analogously, this sample is capable of forming surface OH groups of exceptional thermal stability. This corresponds indeed to the predictions of the kinetic model.

As result of the present study, a hypothesis can be set up which relates the exceptional stability of OH-groups for the sample $x = 0.1$ to the favoured incorporation of Ca in the near-surface region. The process of Ca incorporation into the CeO_2 host lattice depends on the type of electron conductivity. For *n*-type conductors ($x < 0.1$) a high degree of Ca segregation was observed. There, calcium incorporation possibly disturbs surface stabilisation. Since the surface of the *n*-type conducting mixed oxide phase tends to be depleted in Ca, part of the Ca will be segregated from the surface as separate oxide. Above a certain threshold of calcium concentration, the concentration of oxygen defects becomes high enough to contribute significantly to the surface stabilisation by direct anionic charge reduction. Thus, the incorporation of Ca in the surface region might be thermodynamically favoured. Concerning our experimental findings, the threshold concentration of calcium related to the change between the two different mechanism of surface stabilisation should appear between $x = 0.05$ (surface stabilisation by electron donor sites) and $x = 0.1$ (surface stabilisation by creation of oxygen defects).

The positive outcome of the kinetic model validation encourages further application of steady-state kinetic data analysis without *a priori* assumption of rate-determining surface steps to characterise polycrystalline catalysts. Such studies make it possible to de-convolute overlapping effects of surface and bulk structure and their consequences for catalytic performance. Moreover, the kinetic data evaluation might lead to questions which probably would not be asked if exclusively integral values of conversion and selectivity (as demonstrated in Fig. 9) were related to solid phase properties (e.g., for the stability of surface OH-groups). Thus, the experimental results of conventional catalytic tests for activity and selectivity as shown in Fig. 9 suggest that the selectivity can directly be improved by high concentration of calcium in the CeO_2 lattice. However, the kinetic analysis indicates that increasing CaO content does not lead to improved selectivity under all reaction conditions: Especially at higher oxygen partial pressures, the Ca-rich mixed oxides, which are *p*-type conductors, reveal high steady-state coverage by molecular oxygen. Since the molecular oxygen is responsible for ethane combustion (reaction step 7), the selectivity is predicted to decrease at high CaO content under these conditions. To overcome the barrier of C_2 selectivity, two surface reaction steps have to be suppressed simultaneously—the non-desired oxidation of methyl radicals by lattice oxygen (reaction step 2) and the oxidation of ethane by molecular surface oxygen (reaction step 7). Unfortunately, both steps cannot be controlled independently. The suppression of methyl radical oxidation can be achieved over *p*-type conducting oxide. As mentioned above, these catalysts incorporate molecular oxygen into the lattice at a low rate and, therefore, promote the combustion of ethane. To avoid this effect, high concentrations of oxygen defects have to be generated by doping in parallel to high *p*-type conductivity. Here, on the other hand, it must be ascertained that the oxygen defects in the near surface region are not covered by the dopant component due to surface segregation as it was found for the Ca-rich samples.

Another possible way to improve the yield of C_2 hydrocarbons would be the acceleration of methyl radical formation (reaction step 1) relative to the non-selective reaction steps. Here, enhanced selectivity can be expected since the rate of ethane formation via methyl radical recombination (step 6) is of the second order with respect to CH_3 radical concentration. On the contrary, the rate of the undesired CH_3 combustion (step 2) is first order in the methyl radical concentration.

With respect to this strategy of enhanced oxygen activity for methyl radical formation, the present kinetic analysis indicates a limit as well because the actual driving force of methane dissociation is the formation of stable OH-groups on the surface. In this context, the increase of the intrinsic catalyst activity will unavoidably be compensated by higher stability of surface OH-groups blocking the active oxygen sites under steady-state conditions. Consequently, the only way to accelerate the process of methyl radical formation should be an increase of the active site density.

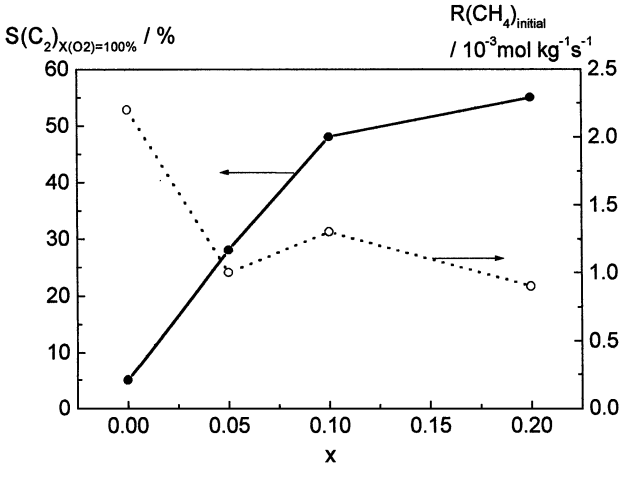

FIG. 9. Experimental data of catalytic tests: C_2-selectivity at 100% oxygen conversion ($T = 993$ K, $p(CH_4)/p(O_2)_{inlet} = 5$) and initial rate of methane conversion at $T = 933$ K, $\tau_{STP} = 0.01$ g s^{-1} ml^{-1}, $p(CH_4)_{inlet} = 50$ kPa, $p(O_2)_{inlet} = 5$kPa.

APPENDIX: NOMENCLATURE

A_{BET}	BET surface area
D	Diffusion coefficient [m^2 s^{-1}]
k_j	rate constant of the jth reaction step [mol · kg^{-1} · s^{-1} · Pa^{-b}]

m_{cat} mass of catalyst [kg]
$\dot{n}$ molar flow [mol s^{-1}]
N_A Avogadro number [number of molecules mol^{-1}]
p_i partial pressure of the component *i* [Pa]
R universal gas constant [$J \cdot K^{-1} \cdot mol^{-1}$]
r_j rate of the *j*th reaction [$mol \cdot kg^{-1} \cdot s^{-1}$]
T temperature [K]
$\dot{V}^0$ total flow rate [$m^3 \cdot s^{-1}$]
Z density of active sites on the catalyst surface [sites $\cdot m^{-2}$]
δ orthogonal distance form the catalyst surface
ε_{cat} porosity of the catalyst bed
ρ_{cat} density of catalyst [$kg \cdot m^{-3}$]
θ_i normalised surface coverage of the component *i*
υ_{ij} stoichiometric coefficient of the component *i* in the *j*th reaction step

ACKNOWLEDGMENT

This work was supported by the Deutsche Forschungsgemeinschaft, which is gratefully acknowledged.

REFERENCES

1. Boudart, M., *Catal. Lett.* **65**, 1 (2000).
2. Ribeiro, F. H., and Somorjai, G. A., in "Handbook of Heterogeneous Catalysis" (G. Ertl, H. Knözinger, and J. Weitkamp, Eds.), p. 771. VCH, Weinheim, 1997.
3. Ilkenhans, T., Herzog, B., Braun, T., and Schlögl, R., *J. Catal.* **153**, 275 (1995).
4. Hinshelwood, C. N., "The Kinetics of Chemical Change in Gaseous Systems," 3rd ed. Oxford Univ. Press, Oxford, 1940.
5. Smith, J. M., *Ind. Eng. Chem. Fundam.* **21**, 327 (1982).
6. Yang, K. H., Hougen, O. A., *Chem. Eng. Prog.* **46**, 146 (1950).
7. Wolf, D., *Catal. Lett.* **27**, 207 (1994).
8. Wolf, D., Moros, R., *Chem. Eng. Sci.*, **52**(7), 1189 (1997).
9. Soick, M., Wolf, D., Baerns, M., *Chem. Eng. Sci.* **55**, 2875 (2000).
10. NAG Group Ltd., NAG Fortran Workstation Library, 1986.
11. Warnatz, J., in "Combustion Chemistry" (W. C. Garnier, Ed.). Springer-Verlog, Berlin 1994.
12. Kvist, A., in "Physics of Electrolytes" (J. H. Hladik, Ed.), Vol. 1, Chap. 8. Academic Press, London, 1972.
13. Gayko, G., Wolf, D., Kondratenko, E. V., Baerns, M., *J. Catal.* **178**, 441 (1998).
14. Shirley, D. A., *Phys. Rev. B* **5**, 4709 (1972).
15. Wagner, C. D., in "Practical Surface Analysis" (D. Briggs and M. P. Seah, Eds.), 2nd ed., Appendix 6. Wiley, New York, 1990.
16. Shyu, J. S., Weber, W. H., Gandhi, H. S., *J. Phys. Chem.* **92**, 4964 (1988).
17. Fujimori, A., *Phys. Rev. B* **27**, 3992 (1983).
18. Wittmaack, K., in "Practical Surface Analysis" (D. Briggs and M. P. Seah, Eds.), 2nd ed., Vol. 2, p. 105. Wiley, New York, 1992.
19. Heber, M., Grünert, W., *Stud. Surf. Sci. Catal. D* **130**, 3279 (2000).
20. Blumenthal, R. N., Brugner, F. S., Garnier, J. E., *J. Electrochem. Soc.* **120**(9), 1230 (1973).
21. Hurley, M. D., Hohnke, D. K., *J. Phys. Chem. Solids* **41**, 1349 (1980).
22. Wagner, C. D., in "Practical Surface Analysis" (D. Briggs and M. P. Seah, Eds.), 2nd ed., Appendix 5. Wiley, New York, 1990.
23. Horrell, B. A., Cocke, D. L., *Catal. Rev.-Sci. Eng.* **29**, 447 (1987).
24. White, D., Hutchison, J. L., Ramdas, S., in "Electron Microscopy and Analysis" (L. M. Brown, Ed.), Inst. Phys. Conf. Ser., Vol. 90, p. 249. Inst. Phys., London-bristol, 1988.
25. Cochrane, H. D., Hutchison, J. L., White, D., *Ultramicroscopy* **31**, 138 (1989).
26. Conesa, J. C., *Surf. Sci.* **339**, 337 (1995).
27. Laachir, A., Perrichon, V., Badri, A., Lamotte, J., Catherine, E., Lavallery, J. C., el Fallah, J., Hilaire, L., le Normand, F., Quemere, E., Sauvion, G. N., Touret, O., *J. Chem. Soc., Faraday Trans.* **87**(10), 1601 (1991).
28. Bernal, S., Calvino, J. J., Cifredo, G. A., Gatica, J. M., Perez Omil, J. A., Pintado, J. M., *J. Chem. Soc. Faraday Trans.* **89**(18), 3499 (1993).